134
4/12/78

DR-2004

UCRL-50028-77-4

H-DIVISION QUARTERLY REPORT

MASTER

October through December 1977

February 10, 1978

Work performed under the auspices of the U.S. Department of Energy by the UCLLL under contract number W-7405-ENG-48.

LAWRENCE LIVERMORE LABORATORY
University of California/Livermore

Distribution Category
UC-34

LAWRENCE LIVERMORE LABORATORY
University of California/Livermore, California/94550

UCRL-50028-77-4

H-DIVISION QUARTERLY REPORT

October through December 1977

MS. date: February 10, 1978

PREFACE

The quarterly report has two purposes: to define the objectives of the five groups in H Division of the Physics Department, and to describe the status of the projects under way.

This report is divided into four sections, each beginning with a summary of the goals and current work of each of the groups reporting in the fourth quarter—Theoretical EOS, Experimental Physics, Code Development, and Fluid Mechanics.

References and experimental details are kept to a minimum in descriptions of the research. However, readers who would like additional information are encouraged to contact individuals engaged in the projects.

H-Division quarterly reports before January 1975 were numbered UCID-16457-72, -3, and -4. Beginning with the quarter for January through March 1975, the reports are series-numbered starting with UCRL-50028-75-1, where 75 is the year and 1 is the quarter.

CONTENTS

H-DIVISION QUARTERLY REPORT

October through December 1977

I. THEORETICAL EOS GROUP

(H. C. Graboske, Group Leader)

The Theoretical EOS Group has two primary tasks: to develop theoretical techniques for describing material properties under extreme conditions, and to construct equation-of-state (EOS) tables for specific LLL materials applications.

Lithium Equation of State

(D. A. Young, M. Ross, and F. J. Rogers)

● **A more accurate lithium EOS was developed for laser fusion reactor application. The EOS includes soft-sphere, pseudopotential, and ACTEX model components.**

Recent proposals for the design of laser fusion reactors have called for blankets or falling curtains of liquid lithium to absorb the energy released in the explosion of the fuel pellet. The lithium absorbs energetic charged particles and radiation in a thin layer on its surface; it absorbs neutrons throughout its bulk.

To simulate the dynamics of the curtain as energy is absorbed, an accurate equation of state is required. Accurate representation of both compressed and expanded states is needed, because the hot surface layer will expand inward toward the center of the reactor, while a shock wave travels outward through the curtain.

For the complete lithium EOS, we have chosen a range of densities from the ideal gas (10^{-4} g/cm^3) to fourfold compression (2.0 g/cm^3), and from the melting point (0.0391 eV) to 31 600 eV.

The components of the tabular EOS include the soft-sphere, pseudopotential, and ACTEX models.

The soft-sphere model[1] is a van der Waals EOS designed to be accurate at low temperatures over the density range from the ideal gas to the dense liquid. It is fitted to experimental liquid lithium thermodynamic data.

In the pseudopotential model,[2] a model interionic potential is computed that assumes a nearly free electron gas. The model potential, together with standard statistical-mechanical fluid perturbation theory, yields an EOS accurate for compressed and moderately expanded liquid up to 50 eV. The predicted shock Hugoniot is in good agreement with experiment.

ACTEX[3] is the standard H-Division EOS code for partially ionized fluids. It is most accurate at high temperatures and low densities.

The total EOS is generated by combining the three model data bases. The regions of overlap between the different models were carefully studied to determine the boundaries of optimum agreement. The final boundaries of the EOS models are shown in Fig. 1. The agreement between models along the boundaries is surprisingly good, showing that the physics is adequate. As usual, however, there is a region in the dense, partially ionized fluid where none of the models is adequate. This was filled by interpolation.

The resulting pressure and energy surfaces are now relatively smooth and well-behaved, except that they are not thermodynamically consistent with one another along the model boundaries and in the interpolation region. This means, for example, that adiabats passing through this region will depend on the method used to compute them. To correct this dependency, we have used the XTENDR code to force the energy surface into consistency with the pressure in the interpolation region. The final EOS now shows very good thermodynamic consistency, but at the expense of unrealistic heat capacity behavior. This tradeoff is probably acceptable, because the fusion reactor simulations do not access the region of unrealistic behavior.

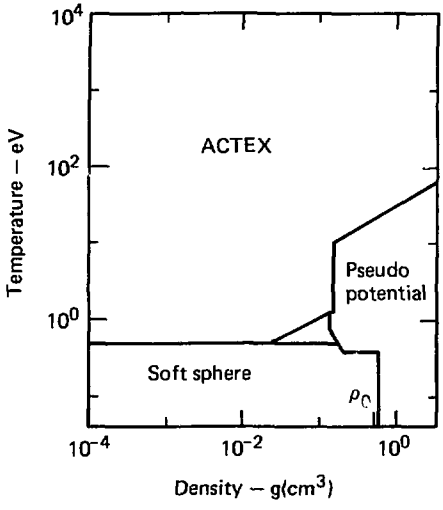

Fig. 1. The density-temperature plane for the lithium EOS. Regions of the three model equations of state are shown; The shaded portion is a gap where none of the models is valid.

Plasma Equation of State

(F. J. Rogers)

● **This section summarizes some extensions of quantum perturbation theory for equilibrium plasma. Included are (1) a rigorous extension of the ring sum to include higher-order diffraction and degeneracy corrections and (2) a pseudopotential procedure to calculate high-order perturbation terms.**

The equilibrium properties of complex plasmas, i.e., incompletely ionized plasmas, is of considerable general interest. The high temperature involved has thus far prevented significant experimental work, so most of our knowledge of these properties comes from theoretical studies. Since the formation of composite particles out of a plasma involves real rather than mathematical clusters, an activity expansion is the natural way to approach the problem. The zero-order term in this expansion is equivalent to the Saha equation, except that rather than using an ad hoc cutoff procedure, the bound-state divergence is eliminated through the analytic properties of the complete set of states.[4] The higher-order terms correspond to two-body, three-body, etc., interactions among all the particles present at a given temperature and density. We will summarize several extensions of the theory.

Diffraction and Degeneracy Corrections to the Ring Sum

The ring diagrams give the leading interacting correction to the Saha equation, the Debye-Huckel correction. In the classical limit, the sum over these diagrams is given by

$$S_C = \sum_i \Lambda_i/3 = 1/12\pi\lambda_D^3 ,$$

$$\Lambda_i = \beta\xi_i^2/\lambda_D ,$$

where

$$\lambda_D = \left[4\pi\beta \sum_i \xi_i^2 \rho_i\right]^{-1/2} \quad \text{is the screening length,}$$

ξ_i = charge on species i ,

ρ_i = density of species i . (1)

However, at sufficiently high density and/or low temperature, diffraction and/or degeneracy effects modify Eq. (1). Diffraction connections enter through the parameter $\gamma = \lambda\!\!\!^{-}/\lambda_D$ and are significant when $\gamma > 0.3$. Degeneracy connections enter through the parameter $\alpha_e = -\mu_e/kt$ and are important when $\alpha_e > -2$.

Using expressions given by DeWitt[5] to evaluate the ring contribution at each order for a Debye potential, it has been shown that the ring diagrams separate naturally into a many-body part and a few-body part. Expansions in γ and α_e that extend DeWitt's results have been obtained.

Pseudopotential Method for Obtaining High-Order Perturbation Terms

Rigorous quantum perturbation expressions are difficult for more complex diagrams than those of ring type. Because of this, a pseudopotential procedure has been developed. To study the compensation between bound and scattering states for n-body interactions, the following parameterized Debye potential was used:

$$U_{eff}(r, D, \lambda\!\!\!^{-}_{ij}) = \xi_i\xi_j \left(e^{-r/D} - e^{-C(\gamma_{D,ij})r/\lambda_{ij}}\right)/r , \quad (2)$$

where

$$\lambda_{ij} = \hbar/\sqrt{2\,\mu_{ij}kT}\,, \qquad \gamma'_{ij} = \lambda_{ij}/D\,,$$

where D is a screening parameter and the function C in Eq. (2) has the form

$$C = C_0/\left[-1 + \sum_1^\infty a_\nu \left(\gamma'_{ij}\right)^\nu\right], \tag{3}$$

and the parameters C_0 and a_ν were determined from the exact second-order perturbation result. [4] Using exact results for high-order two-body perturbation terms, applicable to the limit $\gamma_{ij} \to 0$, i.e. the Coulomb limit, it was shown that C_0 changes slowly with increasing order. This suggests that the a_ν are also reasonably order-independent and that high-order perturbation terms can be obtained from the potential of Eq. (2) with $C(\gamma_{D,ij})$ determined from second-order theory.

The form of Eq. (2) makes it possible to work out analytic expressions at all orders of perturbation theory. This has been done for both two- and three-body terms. Furthermore, using rigorous results as a guide, refinements of the procedure can be developed to improve the results and to determine still higher terms. The few-body perturbation terms using Eqs. (2) and (3) can be turned into a corresponding many-body result, because in the limit $D \to \infty$ the sum over all diagrams derivable from the prototype diagrams gives [6]

$$U_{eff}(r,\lambda_D,\lambda_{ij}) = \xi_i\,\xi_j\epsilon^{-1}(e^{-\alpha_-} - e^{-\alpha_+})/r\,, \tag{4}$$

where

$$\alpha_\pm = \frac{C_0}{\sqrt{2}\lambda_{ij}}\,(1 \mp \epsilon)^{1/2}\,,$$

$$\epsilon = \sqrt{1 - 4\lambda_{ij}^2/C_0^2\,\lambda_D^2}\,.$$

Equation (4) has exactly the same dependence as Eq. (2), and thus the perturbation terms for this potential are the same as Eq. (2) with the substitutions $1/D \to \alpha_-$, $C/\lambda_{ij} \to \alpha_+$ and $\xi_i\xi_j \to \xi_i\xi_j\epsilon^{-1}$.

A formal report on the developments summarized here has been prepared and will shortly be available for distribution.

Improved Ion Corrections to the TFK Theory

(F. H. Ree and D. W. Daniel)

● A code that evaluates improved ion corrections to the Thomas-Fermi-Kirzhnitz theory has been developed. At low temperature, the code uses a Grüneisenlike theory based on Grover's scaling relation and the Grüneisen gamma (γG) that reproduces the available data at low density and Kopyshev's γG at high density. An interpolant smoothly joins the low temperature data with the one-component plasma data at high temperature.

At present, the ionic contributions in the Thomas-Fermi-Kirhznitz (TFK) code [7] are calculated by the one-component plasma (OCP) model. [8] The OCP model assumes that ions of the effective charge Z_{eff} (calculated in TFK) interact by the Coulombic force under a uniform background charge of Z_{eff} free electrons per ion.

Such a model encounters both theoretical and practical difficulties. Theoretically, except at extremely high density or high temperature, free electrons are never uniformly distributed. Instead, they tend to cluster around the positive ions, thus providing a dielectric screening to the otherwise Coulombic ion-ion potential. In practice, this deficiency and the other corrections (shell structure effect, etc.) not in the TFK formalism make it difficult to smoothly join the TFK data with the data obtained from the other physical model (such as GRAY [9]) which is more suitable for lower densities.

To reduce this difficulty, we developed a code, NUC. The code evaluates the ionic contributions to the pressure (P) and energy (E) by using Grover's scaling relations. [10] The scaling relation requires γ_G. We use a physically reasonable expression for γ_G by means of two input densities (ρ_1 and ρ_2) as follows:

$$\gamma_G = \frac{\gamma_0 + a_1\mu + a_2\mu^2 + a_3\mu^3}{1 + b_1\mu + b_2\mu^2 + b_3\mu^3}\,, \quad \rho \leqslant \rho_1\,, \tag{5a}$$

$$= c_1 + c_2\rho + c_3\rho^2 + c_4\rho^3 + c_5\rho^4\,,$$

$$\rho_1 \leqslant \rho \leqslant \rho_2\,, \tag{5b}$$

$$= 0.5 + d_1\rho^{-1/3} + d_2\rho^{-2/3} + d_3\rho$$

$$+ d_4\rho^{-4/3} + d_5\rho^{-5/3} \quad , \rho_2 \leqslant \rho, \quad (5c)$$

where $\mu \equiv \rho/\rho_0^{-1}$ (ρ_0 = reference density).

In Eq. (5a), the coefficients γ_0, a_i, and b_i (i = 1, 2, and 3) are determined from GRAY calculations that will reproduce the best fits to available physical data. The constants d_i (i = 1, ... ,5) have been determined by a least-square fit to Kopyshev's γ_G.[11] Kopyshev's γ_G was first used by Grover,[12] who has also considered improving the nuclear corrections in an H-Division EOS code, MASTER. Kopyshev calculated γ_G by displacing the ions by small amounts, and by calculating the change in the resulting lattice potential under the Thomas-Fermi approximation. The five constants c_1, c_2, ..., c_5 in Eq. (5b) are obtained from four constraints (continuity of γ_G and $d\gamma_G/d_\rho$ at ρ_1 and ρ_2) and Lindemann melting rule,

$$d\ln T_m/d\ln\rho = 2\left(\gamma_G - \frac{1}{3}\right), \quad (6)$$

where T_m is the melting temperature (i.e., average of temperature at the liquidus and the solidus) at fixed ρ. For $\rho \geqslant \rho_2$, we integrate Eq. (6) from the high-density limit

$$T_m = T_m^{OCP} \exp\left[-2\int_\rho^\infty \left(\gamma_G - \frac{1}{2}\right)\rho^{-1}\, d_\rho\right], \quad (7)$$

where T_m^{OCP} is the OCP melting temperature, which is known from Hansen's Monte Carlo computation..[13]

With these expressions for γ_G and T_m, the solid-state data ($T < T_m$) at fixed ρ are obtained under the harmonic-lattice approximation ($P = \gamma_G\rho E$ and $E = 3RT$) and the liquid-state data ($T \geqslant T_m$) from the scaling relation. Further improvements (the Debye model, finite melting region, etc.) that are easy to implement are not considered necessary because they are small. In addition, the ionic contributions are usually a small part of the total P and E, except at low $\rho(\lesssim 1.5\ \rho_0)$ and low T.

Since the above description based on the Grüneisen model would not be appropriate to use at very high temperature ($>>T_m$), we employ the OCP model and interpolate the interconnecting region by using the following formula:

$$P = P^{OCP} + (P^{GK} - P^{OCP})/f(T), \quad (8a)$$

$$E = E^{OCP} + (E^{GK} - E^{OCP})/f(T), \quad (8b)$$

$$f(T) = 1 + \left[T/(30\ T_m)\right]^2, \quad (8c)$$

where the superscripts GK denote the GRAY-Kopyshev description just cited. The P^{OCP} and E^{OCP} from the OCP model are calculated in the TFK code.

Thermodynamic inconsistencies occur in the preceding model because the OCP model,[8] the interpolation formula [Eq. (8)], and the zero-density gap along the melting line were used. However, since the magnitudes of the inconsistencies are usually small, and since the model is to be used in conjunction with the TFK theory, we did not attempt to refine it.

Calculations performed by using this model gave encouraging results for several metals. For example, at T = 4000 K and $\rho = \rho_0$ for Li, P^K [$= P^{GK}$ using Kopyshev γ_G, Eq. (5)] = 5.3 GPa and P^{OCP} = 3.3 GPa compared with the unpublished pseudopotential data P^{PSU} = 5.7 GPa obtained by Ross, while, at T = 1 eV and $\rho = \rho_0$, P^K = 12.3 GPa and P^{OCP} = 8.7 GPa compared with P^{PSU} = 14.5 GPa.

We acknowledge R. Grover for suggesting the use of Kopyshev γ_G and the interpolation function f(T).

Theoretical Estimates of High Pressure Melting in Metals

(H. C. Graboske, K. L. Wong, and R. Grover)

● **A theoretical model study has been performed to predict the phase-transformation loci of seven metals at high pressure. The locations and intersections of physical process paths, Hugoniots and adiabats, with the liquidus, solidus, and coexistence curves, can be determined from the GRAY-model EOS.**

The phase transformations achieved by metals upon shock loading, and the subsequent release are important in constructing accurate equations of state for hydrodynamic simulation codes. The phase changes of primary interest are melting and vaporization, the former under shock compression

and isentropic expansion during unloading, the latter under release only. The GRAY EOS code [14,15] has been developed as an empirical EOS modeling tool to study metals in the three-phase region, and in compression and expansion, with the goal of creating a wide-range equation of state that accurately reproduces all the available experimental thermodynamic-state data for each metal. We have carried out a set of survey calculations, using GRAY for a series of metals ranging from Al to U, to lay out a preliminary estimate of the locations of the high pressure phase boundaries (liquidus, solidus, and coexistence curves).

The theoretical approach to calculate high pressure EOS and phase-transition loci utilized the GRAY code developed by Grover, Royce, and Young. This empirical model code uses a combination of experimental data and composite theoretical models to construct a complete, consistent thermodynamic-state description. The GRAY code treats the atomic, or nuclear contribution by a series of theoretical models covering the entire ρ, T plane: the solid phase (Mie-Grüneisen), the melt (Lindemann law), the hot liquid (scaling law), the high temperature gas (ideal atom gas), the expanded liquid (Young-Alder hard-sphere plus mean-field attraction) and liquid-vapor, solid-vapor coexistence regions (ideal two phase).

To the atomic theoretical model is added the contribution from the effective electron fluid. This can be treated in various levels of approximation, from a low temperature linearized limit to complicated volume-dependent multiple-band models based on band theoretical calculations. In addition to this systematic sequence of theoretical models, the entire model requires a large amount of experimental data for each metal, which then is used as input and test data for the composite model.

The necessary experimental data consist of normal-state data, such as normal density ρ_0, sound velocity c_0, Grüneisen parameters γ_0, a, and electron specific heat g_e; also used are thermochemical data, the detailed information on the expanded hot metal at atmospheric pressure. High pressure static data are used where available for isothermal (static press) data up to pressures in the 1-to-50-GPa range defining the 300-K isotherm. Also available for certain metals are isobaric expansion data (IEX), new LLL experiments where various thermodynamic properties are dynamically measured in expansion at static pressures in the 0.1-to-1-GPa range. Most important are the high pressure Hugoniot experimental data, which provide the key test for theoretical accuracy at pressures up to roughly 5 Mbar (0.5 TPa). With this complete set of experimental constraints available, an appropriate set of theoretical models is chosen. The key input data for the atomic contribution are the form of $\gamma_G(V)$, which is derivable from the zero-K curve, the Hugoniot relation $U_s(U_p)$, taken from experiment, the normal-state data which ensure that the material EOS is correct in the low pressure regime, and the melting and liquid data (T_m, E_{coh}, b_v).

Using GRAY, a complete EOS was constructed for seven metals covering a wide range of atomic weights: Al(27), Fe(55) Brass(68) Ta(181), W(184), Pb(207), U(238). For all these metals, good quality high pressure Hugoniot is available, and for Ta, W, Pb, and U, excellent IEX data have recently been obtained. Because of the complexity of performing a high-order GRAY calculation that reproduces all relevant experimental data with high accuracy, we performed a preliminary survey where only reasonable or approximate agreement was achieved. For this survey, the simpler, low-T forms of the atom and electron models were used, except for Ta and W where more complex models were investigated. The type of agreement of theoretical calculation with experiment is shown in Figs. 2, 3, and 4, and in Table I. The agreement with Hugoniot data is usually best, as shown in Fig. 2, while matches to the thermochemical data, Fig. 3, and isobaric expansion data, Fig. 4, depend on how well the low-order liquid and L-V coexistence

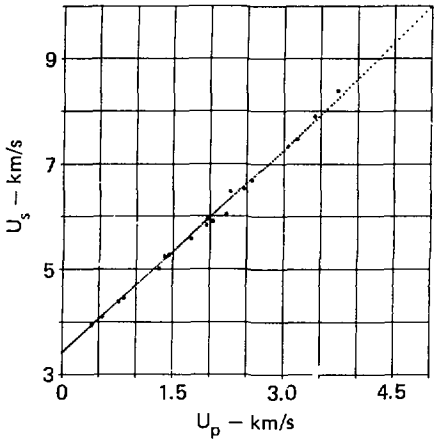

Fig. 2. The tantalum principal Hugoniot, u_s vs u_p. Comparison of the theoretical Hugoniot (trace) and experimental shock wave data (asterisks).

models suit the particular metal, as well as on the time and effort spent in adjusting the expansion ($\rho < \rho_0$) models. A more quantitative evaluation can be obtained from Table 1, where agreement ranges from excellent (Ta, Pb) to poor (Fe, U). In Table 1 certain melt densities (Ta, W) and all critical temperatures have been estimated from independent, systematic studies.[16, 17]

Once a final thermodynamic model has been established, it is instructive to examine certain key thermodynamic paths, and to investigate their intersections. For example, five key-state paths are (1)

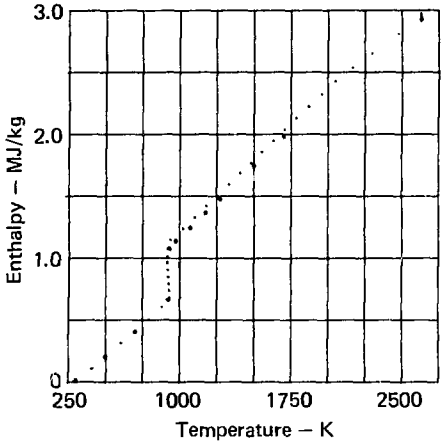

Fig. 3. The aluminum high temperature experimental data for heat content, H(MJ/kg) vs temperature (K) at 1 atm (101 KPa) (shown as asterisks) compared with the theoretical 1 atm (101 KPa) isober (trace).

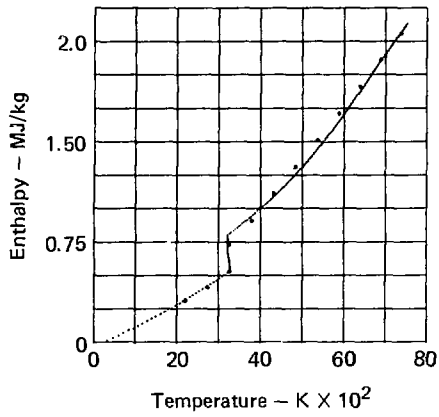

Fig. 4. Tantalum high pressure expansion data at 1 kbar (0.1 GPa), H vs temperature (shown as asterisks) compared with the theoretical 1 kbar (0.1 GPa) isobar (trace).

Table 1. Comparison of theoretical and experimental phase transition.

	T_b^{expt}	T_b^{GRAY}	ρ_{melt}^{expt}	ρ_{melt}^{GRAY}	$T_m^{V\text{-}A}$ [b]	T_m^{GRAY}
Al	2 333	2 300	2.38	2.578	7 151	9 320
Brass	2 152[a]	1 919	Cu = 8.00 Zn = 6.58	7.968	Cu = 7 625 Zn = 3 170	7 738
Fe(304SS)	3 160(Fe)	3 492	7.03	7.204	9 340	15 160
Ta	5 760	5 541	15.0[b]	15.30	17 329	18 800
W	6 000	6 939	17.5[b]	18.34	15 338	25 040
Pb	2 022	2 014	10.67	11.02	4 668	4 665
U	3 550	4 287	17.27	18.02	13 043	24 060

[a] Calculated from wt% average of $T_{boil\ Cu}$ = 2811, $T_{boil\ Zn}$ = 1175.

[b] It should be noted that the entries in Table 1 marked by a superscript b are estimated quantities. Steinberg's method was used to estimate ρ_m for Ta and W, while the Young-Adler method was used to estimate all the metal critical points.

the principal Hugoniot, (2) the principal adiabat, (3) the solidus, (4) the liquidus, and (5) the liquid-vapor coexistence curve. These five curves are shown in Fig. 5 for aluminum, over the pressure range 10^{-6} to 10 Mbar (10^{-4} to 10^{-3} GPa). The relation of the three-phase boundaries (3, 4, 5) and the two physical process paths (1 and 2) are evident. The intersection of these loci is of some theoretical interest, specifically the intersection of the Hugoniot with the solidus and liquidus, representing the onset and completion of shock melting. A higher resolution view of this region is given in Fig. 6 for aluminum. The Hugoniot enters the melt region at 1.1 Mbar (110 GPa) and passes into the fully liquid phase at 1.48 Mbar (148 GPa). Once the complete EOS is available any combination of thermodynamic theoretical paths can be investigated. For example, one might ask to what pressure aluminum must be shock compressed, so that its free expansion upon release will pass through the critical point. Using the EOS developed with GRAY, we estimate a value of 1.9 Mbar (190 GPa) for this case. The pressure and density values for these three intersections (onset of shock melting, completion of shock melting, and shock-compressed state which adiabatically expands through the critical point) are tabulated in Table 2 for seven metals. The pressure required for onset of melting on the Hugoniot ranges from 0.5 Mbar (50 GPa) in Pb to 4.7 Mbar (470 GPa) in W.

A more complete description of this work is available in an internal report to be published that details the input physical data for the GRAY calculations, and gives more complete description of the intersection and locations of the various thermodynamic loci.

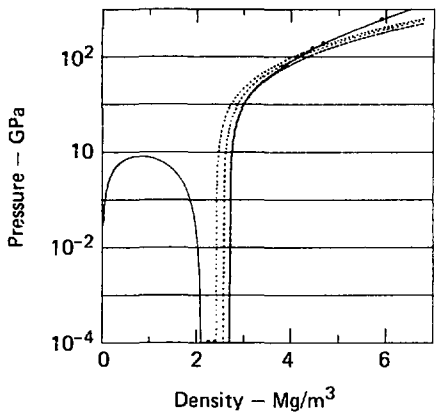

Fig. 5. The pressure-density plane for aluminum showing the five key paths: principal Hugoniot, principal adiabat, liquidus, solidus, and coexistence curve with various intersection points.

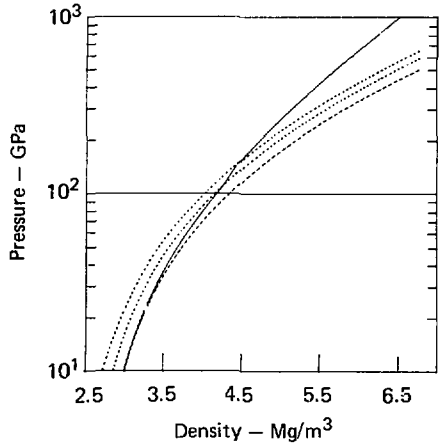

Fig. 6. A high resolution plot of the pressure-density plane for aluminum, showing the Hugoniot passing through the solidus and liquidus, and the principal adiabat.

Table 2. Intersection of Hugoniots with various phase lines.

Locus		Material						
		Al	Brass	Fe(SS304)	Ta	W	Pb	U
Onset of shock melting	P	1.095	1.743	4.65	2.856	4.685	0.507	1.957
	ρ	4.24	13.12	13.47	26.92	31.83	16.12	29.22
Completion of shock melting	P	1.482	1.947	6.30	3.480	5.70	0.64	2.645
	ρ	4.443	13.33	13.84	28.18	32.90	16.65	30.19
Intersection of isentrope from the critical point with the Hugoniot	P	5.959	6.304	15.31	–	–	24.73	–
	ρ	5.891	16.57	15.97	–	–	21.87	–

II. EXPERIMENTAL PHYSICS GROUP

(J. W. Shaner, Group Leader)

The experimental Physics Group investigates the properties of materials at extreme conditions of pressure and temperature and develops new techniques in performing these investigations. In addition, studies are carried out on the response of materials to a wide range of dynamic pressures and temperatures. These activities provide information for both theoretical EOS and computer-simulation efforts.

Parabolic Projectile Distortion in the Two-Stage Light-Gas Gun

(W. J. Nellis and A. C. Mitchell)

● A shock-wave detection system with a time resolution of ~0.3 ns was used to measure the shape of the impacting surface of 2-mm-thick Ta impactor plates used for Hugoniot measurements. It was found that these impactor plates undergo parabolic distortion that can cause errors on the order of 5% in shock-velocity measurements if not taken into account properly.

Equation-of-state data at high pressures and temperatures can be obtained by the shock-impedance matching method. In this method, shock-wave velocities in the material under study, and the known EOS of a standard material are used to calculate thermodynamic properties. Error propagation can be significant because the uncertainty in volume, for example, is typically two to three times the uncertainty in shock velocity. Thus, a fast response time detection system having a time resolution of 0.3 ns was developed to perform accurate shock-wave velocity measurements. This system has now been used to measure the shape of the impacting surface of 2-mm-thick Ta impactor plates. The purpose is to determine the spatial profile of the shock wave so that deviations from planarity can be taken into account in the Hugoniot data analysis.

Projectiles are made by hot-pressing a metal plate into a polycarbonate cylinder that is machined to fit into a polyethylene gas seal. The entire assembly is then machined for a close slip-fit into the launch tube of a two-stage light-gas gun.[18] The targets had 13 detectors arranged in a cross configuration and mounted against a 1-mm-thick Ta plate. The pin separation was generally 3.0 ± 0.1 mm or better. The detector configuration is illustrated in Fig. 7. It has long been known that projectiles emerging from the launch tube are tilted through an angle of ~1°. In the LLL two-stage gun, both the magnitude and orientation of the tilt are quite reproducible. Thus, some of the targets were rotated before the shot to compensate for projectile tilt. In so doing, both rows of detectors are more sensitive to projectile distortions other than tilt, which can cause up to ~100-ns variation in the arrival time across the target diameter. Experiments were performed as a function of impact velocity, which was varied only by changing the gun powder load.

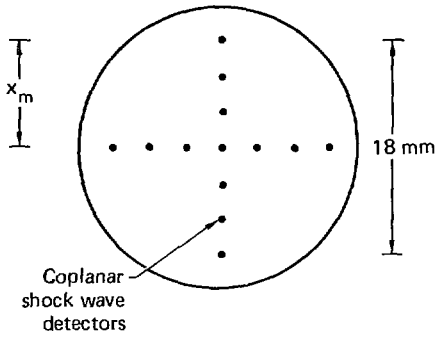

Fig. 7. Coplanar detector arrangement to diagnose projectile distortion.

Ten rows of detectors from seven shots were analyzed in terms of projectile tilt and a concave bowing distortion, both illustrated in Fig. 8. For detectors arranged along the x axis and for parabolic bow, the arrival times, t, of a shock wave are described by

$$U_I t = \tan\theta\,(x_m - x) + a(x_m^2 - x^2), \qquad (9)$$

where U_I is the impactor velocity, θ is the angle between the wave front and the line of detectors, a is the amplitude parameter of the parabola, and x_m is the x coordinate of the outermost detector. Time is referenced to the first signal at t = 0 from the detector at $x = x_m$. The first term in Eq. (9) is due to pure tilt; the second term is due to pure bow.

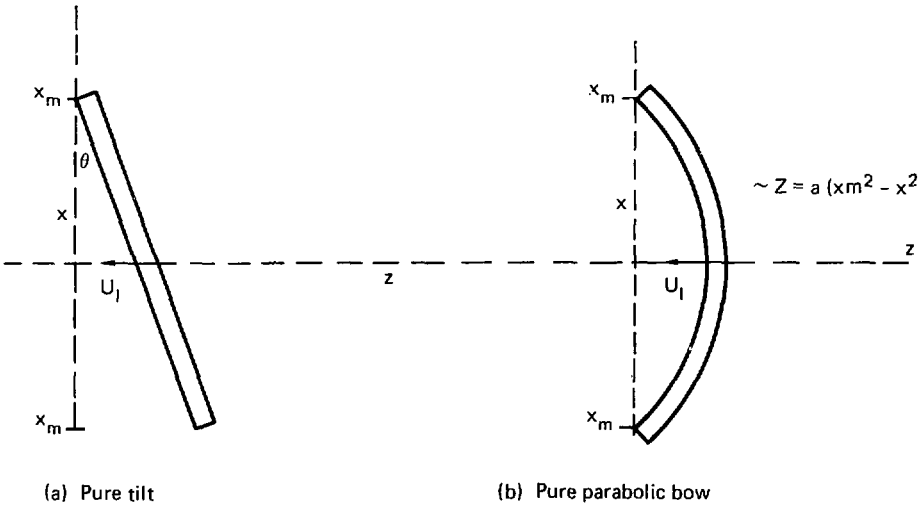

Fig. 8. Schematic illustration of projectile tilt and parabolic bowing distortion.

Because $\theta \simeq 1°$, the two terms simply add. The only unknowns are θ and a, which were obtained by least-squares fitting of the data to Eq. (9).

All the data sets fit Eq. (9). The average standard deviation from the fits for the 10 data sets was 0.91 ns, with a range of 0.25 to 1.57 ns. The standard deviation was taken as $[\Sigma d_i^2/(N-3)]^{1/2}$, where d_i is the deviation of a given data point from the fit, and N is the number of data points. N was reduced by 3 to calculate the standard deviation because the fit is constrained to go through the first data point at $t \equiv 0$ and a minimum of two more data points is required to determine the two fitting parameters. All measured arrival times were used in the fitting procedure, and N ranged between 5 and 7 over the 10 data shots.

The a parameter is plotted vs projectile velocity in Fig. 9. It can be seen that there is a monotomic increase in parabolic distortion up to a velocity of 6.3 mm/μs then the distortion roughly doubles. A bowing parameter of 1.3×10^{-3}/mm causes a time difference of 16 ns between the center and 9-mm radius of the outermost detector at $U_I = 6.5$ mm/s. It was found that 1.5-mm-thick Ta impactor plates undergo smaller parabolic distortion, which increases smoothly up to ~8 ns across a radius at maximum velocity. For this reason only 1.5-mm-thick Ta impactors are now used for Hugoniot measurements.

In our Hugoniot experiments, the detectors on a given plane are arranged on a circle. The detectors on the first plane to register the shock wave are on a

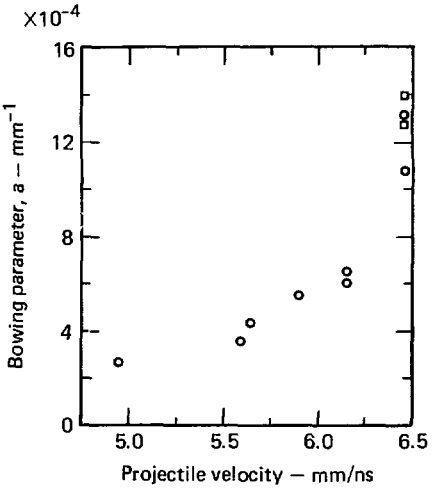

Fig. 9. The parabolic bowing parameter, a, plotted vs projectile velocity for 2-mm thick tantalum impactor plates.

radius about twice that of the second plane of detectors. The parabolic distortion causes the center to lag the outside of the impactor. Thus, there is a time delay between the two planes of detectors due to the bowing. As a result, measured shock transit times will appear longer than is actually the case, and shock velocities will appear smaller. Thus, the error due to bow is systematic and not random. Because the time delay can be up to ~10 ns compared to shock transit times of ~200 ns, it is important to correct for the parabolic distortion. It must be emphasized that these distortions depend in detail on the operating parameters of the two-stage gun, and on the materials and fabrication techniques of the projectiles.

Construction of a Ballistic Range for Long-Rod Penetrators

(J. K. Scudder)

● The long-rod penetrator represents a significant threat to heavy vehicular armor. A Defense Advanced Research Projects Agency (DARPA) sponsored study in H-Division examines, on several absolute-size scales, the performance of these penetrators and their requirements for specific material properties.

Background

A long-rod penetrator (LRP) is an inert, high-density ballistic projectile characterized by a large length-to-diameter ratio and, in use, a high kinetic energy. The LRP is used in military applications to attack heavy vehicular armor. The penetrator is effective because of its enormous kinetic energy, its small target contact area, and because of the long-durection stress that it applies to a target. For example, a 25-mm diam, 250-mm-long tungsten penetrator traveling at 1.5 km/s has a kinetic energy of 2.5 MJ. It takes about 4 kJ to make a 1000-mm ^{3} crater in steel, and so this penetrator could remove about 6×10^5 mm ^{3} (38 in ^{3}) of target. This is a very rough estimate, but suffices to illustrate the importance of the LRP as an anti-armor weapon.

H-Division is now under contract with DARPA to conduct laboratory ballistic tests with scale model long-rod penetrators. The testing to be done investigates two important areas:

- The ability of scale-model results to predict full-scale ballistic performance.
- The importance of specific LRP geometric and material properties during impact and penetration.

Experimental Program

The scale-model penetrators to be fired in our new facility have a mass of 65 g and l/d of 10. Both tungsten-alloy and steel penetrators will be launched with a 23-mm smooth-bore gun. The subcaliber penetrators are sabot-supported during launch and will be fired into an evacuated chamber containing scale models of military armor.

Details of the launch, target impact, and penetration will be recorded with framing camera and multiple-head flash x-ray equipment. After penetration, the residual rod fragments will be arrested in a soft material and recovered later for inspection.

The sensitivity of LRP performance to absolute size will be studied through comparison of data generated with this gun to that obtained with a much smaller gun (now in service), as well as that obtained at full scale by the U.S. Army at Aberdeen Proving Grounds.

Because the cost of experimentation rises rapidly as one approaches full scale, these size-sensitivity tests are very important to the ballistic research community.

Fourth-Quarter Work

This quarter, the design and fabrication of components for the 23-mm gun have proceeded and are now virtually complete. In addition, laboratory tests with the very small-scale LRPs have been conducted.

We have studied the behavior of the miniature penetrators in low-erosion targets (such as aluminum). By "turning off" one or more of the otherwise obscuring damage processes, we get a clearer view of *other* important damage mechanisms.

Next quarter will be devoted to further small-scale tests, as well as the assembly and testing of the new 23-mm gun.

Thermodynamics and Sound Velocities in Liquid Metals

(J. W. Shaner)

● Estimates, based on available thermodynamic data and an empirical electronic density of states, are made for the sound velocities of several liquid metals.

The sound velocity of a material is an important quality for both engineering and thermodynamic applications. Measurements of acoustic velocity for liquid metals has been limited to the low-melting point metals because of experimental difficulties

associated with the high temperatures and reactivity. Calculations based upon available thermodynamic data and reliable models are presented here on the sound velocity of several high-melting point metals.

The bulk sound velocity of liquid can be written as

$$C = \sqrt{B_s V} , \tag{10}$$

where B_s is the adiabatic bulk modulus, and V is the specific volume. By using the relation between the constant volume and constant pressure heat capacities (C_v and C_p, respectively),

$$C_p = C_v + VT\alpha^2 B_T , \tag{11}$$

where α is the volume thermal expansion coefficient, and B_T is the isothermal bulk modulus, we can rewrite the sound velocity as

$$C = \left(\frac{C_p}{\alpha^2 T}\right)\left(\frac{C_p}{C_v} - 1\right) . \tag{12}$$

This form is particularly appropriate with respect to our isobaric expansion experiments (IEX), because all quantities on the right side of Eq. (12) are currently measured, except C_v. We have described a technique to measure the sound velocity.[19] Before these measurements are actually made, it is useful to make the best possible estimate of the values we expect to find. These estimates will help to interpret the sound velocity measurement even in the presence of significant noise on our interferometer signals.

What is needed in Eq. (12), in addition to the measured quantities, is an estimate of C_v.

The particular form chosen for C_v is composed of normal fluid and electronic contributions. The normal fluid part is based on Grover's scaling law [20]:

$$C_v^Q = 3R(1 - A\,T/T_m) , \tag{13}$$

where A is a constant of order 0.05. This form has been shown by Monte Carlo calculations to be a good approximation near the melting point for neutral fluids with a wide variety of pair potentials.[21]

The electronic contribution is of the degenerate electron form:

$$C_v^e = \gamma T . \tag{14}$$

Various values of γ could be chosen. The value determined by heat capacity measurements below 5 K, γ_0, could serve as a starting point, but these values are anomalously high since they are based on an electronic mass which has been enhanced by the electron-photon interaction. This enhancement is expected to disappear above the Debye temperature.[22] Values of γ_0 and the mass enhancement factor $(1 + \lambda)$ are given in Table 3 for several metals of interest for IEX. Here the values of $(1 + \lambda)$ are taken from the McMillan formula[24] relating the mass enhancement to the superconducting transition temperature. The value of γ derived from the band structure density of states at the Fermi surface, γ_0 band, can then be obtained empirically by

$$\gamma_0^{band} = \gamma_0/1 + \lambda) . \tag{15}$$

To compare γ_0 band with the value obtained from band structure calculations, we use the relation for the density of states at the Fermi surface of one spin, N_{bs},

$$N_{bs} = \frac{3\gamma_0^{band}}{2\pi^2 k^2} .$$

Table 3. Electronic thermodynamic properties.

Material	$\gamma_0\left(\frac{MJ}{mole}\,K^2\right)^a$	$(1 + \lambda)^b$	γ_0^{band}	γ_{FEG}
Cu	0.695	1.10[c]	0.63	0.50
Al	1.35	1.38	0.98	0.91
Zn	0.64	1.38	0.46	0.75
Sm	1.80	1.60	1.13	1.41
Pb	3.14	2.12	1.48	1.51
Nb	7.66	1.82	4.21	1.16
Mo	2.10	1.41	1.49	1.11
Ta	5.84	1.77	3.30	1.15
W	1.22	1.15	1.06	1.11
U	10.9	1.90[d]	5.74	1.16

[a]Reference 23.
[b]Reference 24.
[c]Reference 25.
[d]Reference 26.

Where band structure calculations are available, the agreement between calculated and empirical density of states is good, as shown in Table 4.

Table 4. Empirical and calculated density of states for transition metals.

Material	N_{bs} (empirical)	N_{bs} (calc)
Nb	0.91	0.73[a]
Mo	0.28	0.31[b]
Ta	0.77	0.64[a]
W	0.15	0.15[c]

[a]Reference 27.

[b]Reference 28.

[c]Reference 29.

A very naive approach to calculating γ would be to use the free electron gas model. This quantity is

$$\gamma_v^{FEG} = \frac{\pi^2 N K^2 m}{\hbar^2 (3\pi^2\ N/V)^{2/3}}\ v^{1/3}\ , \qquad (16)$$

where v is the valence of the ions, N/V is the ion number density, and m is the free electron mass. Not surprisingly, this quantity agrees with γ_0 band for reasonable valences only in the cases of Pb, Cu, and Al, where all the valence electrons are derived from s and p states. In summary, at least at room temperature and above, the best choice of γ must be γ_0 band.

The implicit temperature dependence of γ must also be included. Because $\gamma^{FEG} \propto V^{2/3}$, we may take $\gamma(T) = \gamma_0\ \text{band}\ [V(T/V_0)]^{2/3}$. Finally, we write

$$C_v = 3R\left(1 - A\,\frac{T}{T_m}\right) + \gamma_0^{band}\left(\frac{V(T)}{V_0}\right)^{2/3} T\ . \qquad (17)$$

This form may be expected to become less accurate as T and V increase because the electron gas becomes less degenerate, and thermal excitation of electrons out of core states becomes important. These effects will be ignored here.

Values of the acoustic velocities calculated by Eq. (12) are presented for a variety of metals in Table 5. The first group is those for which experimental data exist.[30] Considering uncertainties in the thermodynamic quantities used in Eq. (12), the ~20% agreement of calculated and measured sound velocities may be considered reasonable. A notable exception is the case of Al. The value for the thermal expansion coefficient for liquid aluminum,[31] 1.65×10^{-4}, is large compared with the value $\sim 10^{-4}$ found for most simple metals. A high value of α reduces the calculated C. This is a clear case where a confirming measurement of the liquid thermal expansion coefficient is needed. Also surprising are the very high values of C calculated for Nb and Mo—higher in fact than the 300 K solid bulk sound velocities. These high values are probably a result of inaccuracies in the input thermodynamic data, but confirmation will have to wait until we measure the sound velocities. Finally, we note that the sound velocity data will be valuable input for a GRAY equation of state, like that given by Grover for lead,[34] obtained to fit all experimental data.

Isobaric Expansion Measurements on Platinum

(G. R. Gathers and W. M. Hodgson)

● **Preliminary results are presented for the volume expansion and electrical resistivity of platinum vs enthalpy to nearly twofold expanded states.**

The isobaric expansion apparatus[35] has been used to measure equation-of-state and electrical resistivity of platinum. We present here preliminary results of the investigation. Figure 10 shows a plot of enthalpy vs volume for three shots made at 0.2,

Table 5. Acoustic velocity for liquid metals at the melting point.

Material	c (calc),[a] km/s	c(exp)[b]
Cu	3.5	3.5
Al	3.6	4.7
Zn	3.1	2.7
Sn	2.9	2.5
Pb	2.3	1.8
Nb	5.1	
Mo	6.7	
Ta	3.6	
W	2.5	
U	2.4	

[a]Data for these calculations has come from references 31, 32, and 33.

[b]Reference 30.

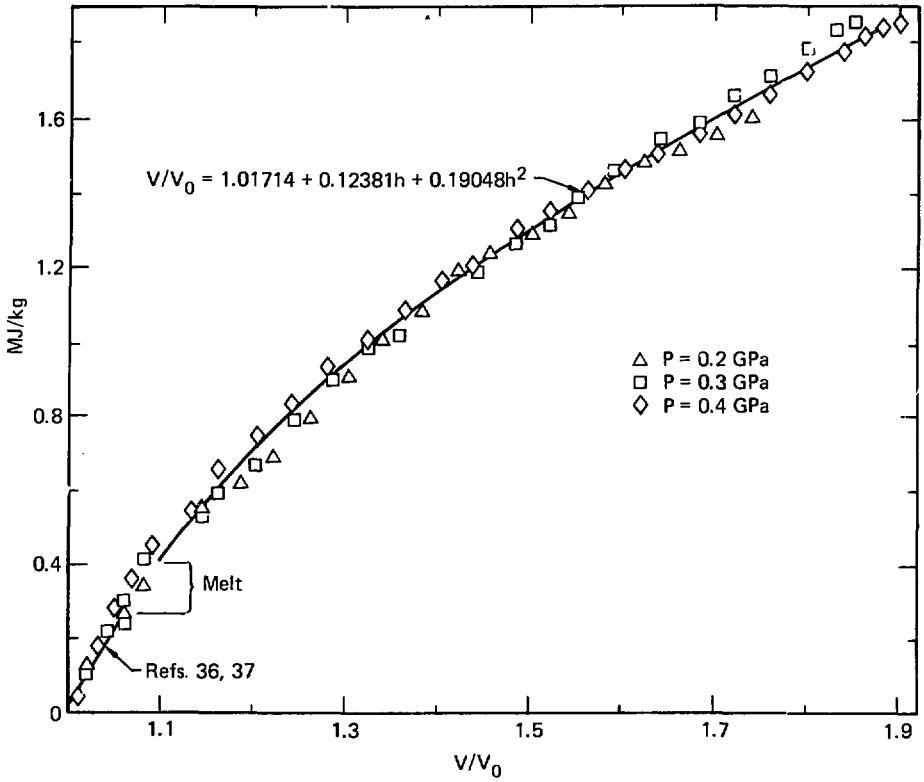

Fig. 10. Volume vs enthalpy for shots taken at 0.2, 0.3, and 0.4 GPa. The enthalpy is referenced to the state at 1 MPa, 298 K.

0.3, and 0.4 GPa. The compressibility is low enough that the isobars cannot be distinguished. The enthalpy is referenced to the state at 0.1 MPa and 298 K. An initial enthalpy input of 0.0172, 0.0257, and 0.0342 MJ/kg is produced by the work done on the sample during pressurization of the cell for shots at 0.2, 0.3, and 0.4 GPa, respectively. Subsequent enthalpy increases from electrical heating are then added to these amounts. A polynomial hand fitted to pass through the cluster of points is

$$V/V_0 = 1.01714 + 0.12381h\ (MJ/kg) + 0.19048h^2\ (MJ/kg)^2 .$$

Hultgren *et al.* (pp. 396-401) [32] give specific heat data for the solid, which may be described by

$$C_p(MJ/kg) = 1.329 \times 10^{-4} + 2.70 \times 10^{-8}\ (T - 298) .$$

Integration then gives

$$h(T) = \int_{298}^{T} C_p\ dT$$

or

$$h(MJ/kg) = 1.329 \times 10^{-4}\ (T - 298) + 1.35 \times 10^{-8}\ (T - 298)^2 .$$

Waseda *et al.* [36] have measured the thermal expansion of the solid by x-ray diffraction techniques. The lattice constant is described by

$$a/a_0 = 1 + 5.546 \times 10^{-6}\ (T - 298) + 3.750 \times 10^{-9}\ (T - 298)^2 .$$

This may be cubed to give the volume ratio v/v_0 for the solid as a function of temperature, and may be used with the above expression for the enthalpy to generate a predicted v/v_0 vs h curve for the solid. The curve is plotted in Fig. 10.

Figure 11 shows a plot of the electrical resistivity vs enthalpy. We have ignored the enthalpy due to compression here. The resistivity in the liquid is described by

$$\rho(\mu\Omega m) = 0.8923 + 0.1512h \text{ (MJ/kg)} + 0.2405h^2 \text{ (MJ/kg)} ,$$

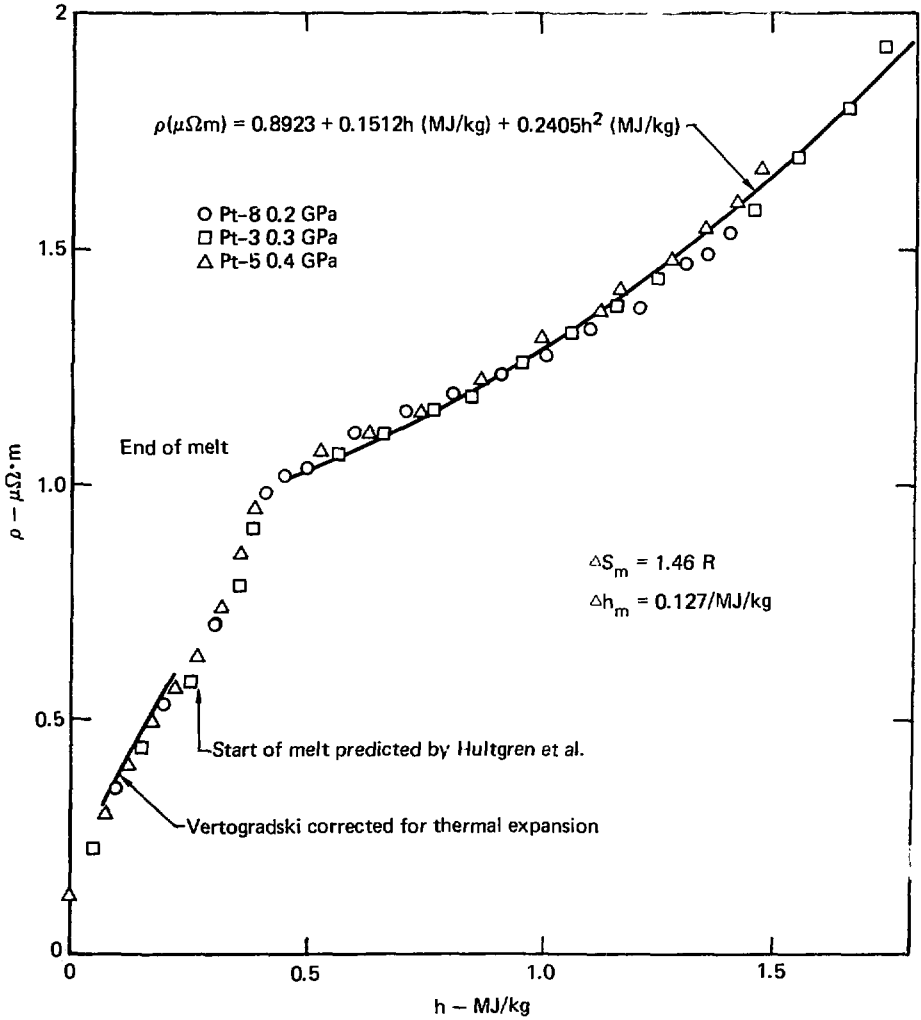

Fig. 11. Electrical resistivity vs enthalpy for shots taken at 0.2, 0.3, and 0.4 GPa. The enthalpy is due to electrical heating only, so the reference state for each shot is 298 K and the ambient cell pressure.

where h is the enthalpy increase due to heating. If we use the results of Hultgren *et al.*, and Waseda *et al.*, and take a melting temperature of 2042 K to predict the beginning of melt and the abrupt kink in ρ to represent end of melt, the heat of fusion is 0.127 MJ/kg and the entropy of melt is 1.46R.

Vertogradskii [37] recently measured the resistivity of platinum from 800 K to 1800 K, expressing the results as

$$\rho(\mu\Omega m) = 0.113 + 0.3976 \times 10^{-3} (T - 273) - 0.526 \times 10^{-7} (T - 273)^2 .$$

This can be converted to the form

$$\rho(\mu\Omega m) = 0.1229 + 3.950 \times 10^{-4} (T - 298) - 5.26 \times 10^{-8} (T - 298)^2 .$$

Vertogradskii did not make corrections for thermal expansion, however. The results of Waseda *et al.* may be used to make the correction. The result is

$$\rho(\mu\Omega m) = 0.1229 + 3.957 \times 10^{-4} (T - 298) - 4.995 \times 10^{-8} (T - 298)^2 + 1.190 \times 10^{-12} (T - 298)^3 - 1.973 \times 10^{-16} (T - 298)^4 .$$

The result is plotted in Fig. 11, using the Hultgren specific heat results to generate the corresponding enthalpy values. Vertogradskii's corrected results lie about 6% above ours.

Because the compressibility of platinum is low, the resistivity and its dependence on temperature is not very sensitive to pressure. In addition, the specific heat C_p should not be affected much by the pressure. Consequently, one should expect rather good agreement with the corrected Soviet results which correspond to atmospheric pressure.

Shaped-Charge Code Development

(M. van Thiel and J. L. Levatin)

• The calculation of jet characteristics is an important part of the shaped-charge design process. Such calculations have been carried out by a number of techniques. The methods are being continually improved as new data become available.

The calculation of the velocity-mass profile of a jet produced by a shaped charge is an important part of shaped-charge design. A simple one-dimensional model for performing this calculation was developed in 1948. [38] With an estimate of the velocity imparted to the shaped-charge liner by the explosive, the model then computes collapse angle liner velocity vector, jet velocity, ano mass.

The more accurate method of using Eulerian or Lagrange codes to calculate jet characteristics directly requires very small zones and is relatively cumbersome. Lagrange calculations can, however—without fine zoning—accurately determine collapse angles (β) (see Fig. 12), liner velocities (V_0), and velocity direction (A) of the center of mass of the liner. These quantities can then be used in the aforementioned model to define jet velocity (V_j) and mass (m_j), as well as corresponding quantities for the slug. This method has been applied to a number of device designs.

A computed curve, labeled old model, is shown in Fig. 12. This is a plot of the jet velocity computed for each liner element plotted vs the original position of the element. The values of β, A, and V_0 are those of the center of mass.

The one-dimensional model does not include the liner compression-decompression (stagnation) process that is caused by collapse of the liner on the axis of the cone. This offers no serious problems as long as the liner is not being accelerated before impact, and if β is not changing with time. The superposition of changes produced in V_0 and β by stagnation processes, and those due to the explosive-liner interaction, introduce an uncertainty in the final liner energy and configuration to be used in the jet formation model. The comparison with experiment given shows that deviations are comparatively large where $\partial V_0/\partial t$ is large, near the apex of the device.

A model that can be used in the range where stagnation pressures are significant is required to correct this problem. We have used the fact that pressures at the free surface of the liner are always zero. All acceleration forces on an infinitely thin-surface element are therefore normal to the surface, and the liner element should retain its original length. The original equation for jet velocity, $V_j = V_0 \cos(A - \beta/2)/\sin(\beta/2)$, could then be applied to the inner zone of the liner element if it were thin enough. However, since efficient Lagrange zoning is generally too coarse to make stagnation pressures negligible, the element length will fluctuate and therefore the jet velocity. A good first-order correction is made with the one-dimensional Rieman

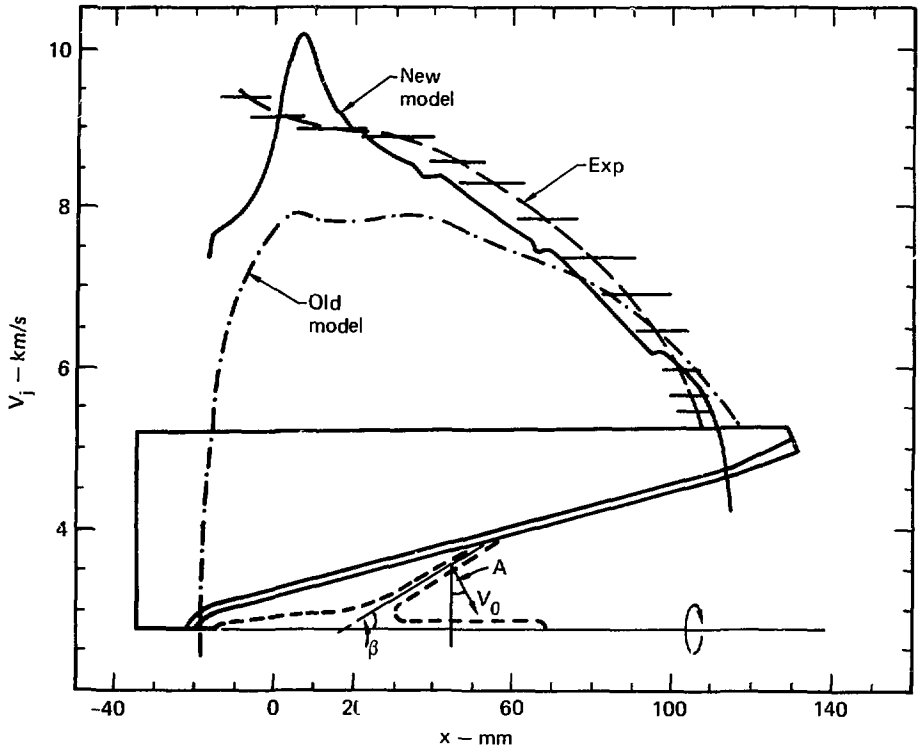

Fig. 12. Jet velocity of the cone elements vs original position (x); exp. ≡ experimental curve. General cone configuration before and during collapse, showing definition of A, β and V_0.

equation. This equation $(\partial V/\partial v = (\partial\sigma/\partial v)^{1/2})$ relating velocity change to the decompression path of the material is justified because the final velocity vector lies totally in the x direction. Decompression acceleration in the radial direction, therefore, need not be considered. The corrected jet velocity is then $V_j(cor) = V_j + \int (\partial\sigma/\partial v)^{1/2} dv$.

The jet mass (m_j), slug mass (m_s), and slug velocity (V_s) were calculated using the three conservation conditions applied to the liner zones of each element (unsubscripted):

Mass: $m_j + m_s = m = \sum m_i$ (sum over all liner zones);

Momentum: $m_i V_i + m_s V_s = \sum m_i x_i$;

Energy: $m_j v_j^2 + m_s v_s^2 = \sum m_i \dot{x}_i^2 + \dot{y}_i^2 + 2 \sum \int_{\sigma_i}^{0} \sigma_i dV$.

The model routine is FSJET42 and operates on the binary output of HEMP.

Figure 13 shows that the new model is insensitive to stagnation pressures. The value of V_j calculated with the new model from a particular liner element is reasonably constant during the stagnation process. The shaded region shows the pressure correction applied. The old model, on the other hand, calculates a value of V_j that dips sharply in

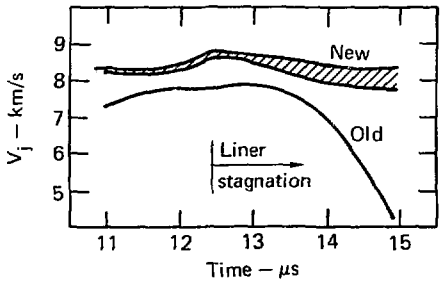

Fig. 13. Calculated jet velocity of a liner element during liner collapse. Old is calculated with the old model. New is calculated with the new model — pressure correction (upper curve); without pressure correction (lower curve).

the stagnation region. As noted this sensitivity to stagnation pressure masks effects produced by rapid liner acceleration or a large velocity gradient ($\partial V_0/\partial x$).

The new model also agrees better with experiment. Figure 12 shows that the calculated values for the liner elements start below the experimental value, then rise through the experimental curve before coming back down to follow closely along the experimental contour. The deviations are not significant for two reasons: the horizontal lines that indicate experimental reproducibility explain most of the difference, and the experimental velocities were taken at about 110 μs. The jet particle trajectories were therefore linearly extrapolated to the formation time and position to yield the comparison. Errors in this linear extrapolation process can account for the remaining deviations.

To avoid the linear extrapolation of the experimental jet velocities, the nonlinear expansion of the jet may be calculated using HEMP. The shape of the Lagrange grid is defined by the radius of each jet element its formation time and length, which are also calculated by FSJET24. The results of this calculation are compared in Fig. 14. The input velocity profile obtained from Fig. 12 is also shown there. Comparing the velocity profile at the time of the formation of the final element (40 μs) shows that the hump in the curve has disappeared and is replaced by a uniform tip velocity. This tip velocity

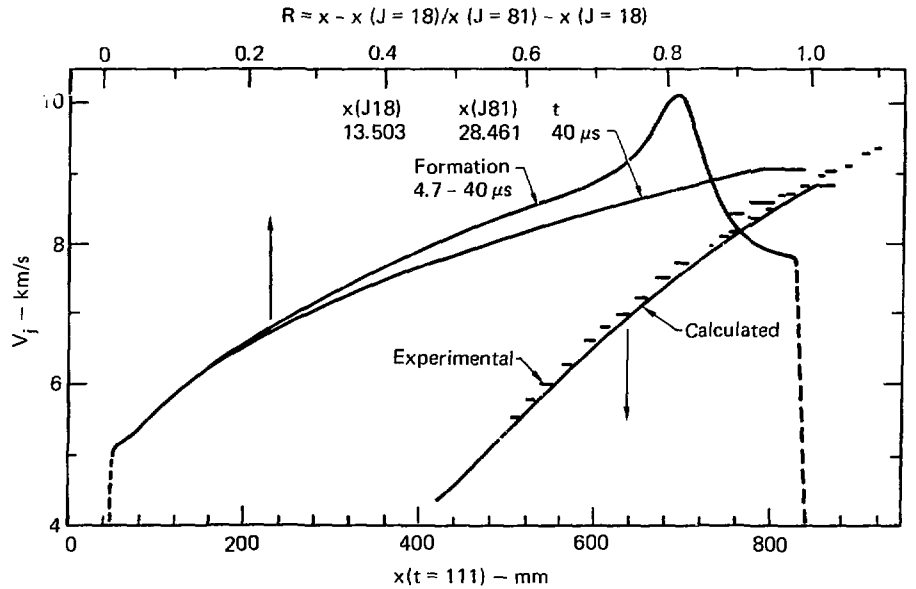

Fig. 14. Jet velocity vs position of the jet elements. Top two curves are vs normalized jet length of the elements at formation time at 40 μs. Lower curves are vs element position at 111 μs (CALC: calculated curve; Exp. experimental element locations).

further decreases under the tensile forces of the material behind it. At the time corresponding to the experimental jet velocity-position profile, this calculated tip velocity is below the experimental value.

Possible causes for this descrepancy could be as follows:

- Too high an estimate of the strength.
- Too coarse zoning to accurately determine the velocity profile of the jet tip at formation time.
- Additional model errors.

A lowering of the 5-kbar strength of this jet would cause the tip to break up. As it is, the size of this tip compares well with the experimental one. The strength is therefore correct. Determination of the two other causes requires further investigation.

III. CODE DEVELOPMENT GROUP

(L. L. Edwards, Group Leader)

The mission of H-Division's Code Development Group is to develop and apply time-dependent fluid mechanics programs. The *motivation* is to develop codes (based on either known or new methods) that will solve general classes of fluid-flow problems.

Presently we are concerned with simulations of the following:

- Nuclear reactor pressure suppression systems.
- Shaped-charge jet formation.
- Weapons effects.

The codes being developed (and/or adapted) include:

- CHAMP (Coupled HEMP and Multifluid Eulerian Program), a homogeneous compressible, explicit finite-difference, coupled Eulerian Lagrangian code.
- PELE, a multimaterial multiphase explicit finite-difference Eulerian code.
- PELEIC, an incompressible explicit finite-difference code based on the MAC methods.
- CHPCODSC, a specialized version of CHAMP for shaped-charge calculations.

PELE Code Development

(W. H. McMaster)

- **Development of the PELE code has been directed toward the solution of problems associated with the pool supression dynamics of a hypothetical loss-of-coolant accident (LOCA) for nuclear reactors.**

The long-range objective has been to develop the capability of handling two-phase coupled fluid dynamics. The first approach toward this objective was the development of two codes, PELE and PELE-1D, which used second-order explicit differencing implemented by alternating one-dimensional sweeps. The alternating one-dimensional sweep technique, which has proven to be very effective in high pressure regimes, was found to be inappropriate for pressures in the range of 1 bar for essentially incompressible fluids such as water. To correct this deficiency, cross-flux advection terms were incorporated into the two-dimensional PELE algorithms. These changes were found to lead to solutions that compared favorably with theoretical and experimental data. However, in the range of low pressures and incompressible fluids, these explicit techniques are extremely inefficient. To pursue the solution to times of interest (many milliseconds), it became necessary to investigate implicit, incompressible algorithms.

The approach taken was to develop a code based on the MAC technique as simplified and implemented in the SOLA codes.[39] The resulting code is called PELEIC, where we have not only incorporated the basic incompressible algorithm of the SOLA codes, but have added a coupling to flexible structures on the boundary of the grid and a void fraction routine to account for bubble growth and motion. The void fraction algorithms are based on concepts previously developed for the MAITAI and PELE codes.

This new code, PELEIC, has been used to compute an experiment performed by Catton *et al.*[40] at UCLA with results that agree quite favorably with the experimental data.

The results of these calculations are shown in Figs. 15-17. In Fig. 15 we show a comparison of the surface motion in the pipe for the compressible and incompressible approaches. In the compressible calculation, the vent clearing occurs approximately 4 ms. later; however, both are within the accuracy

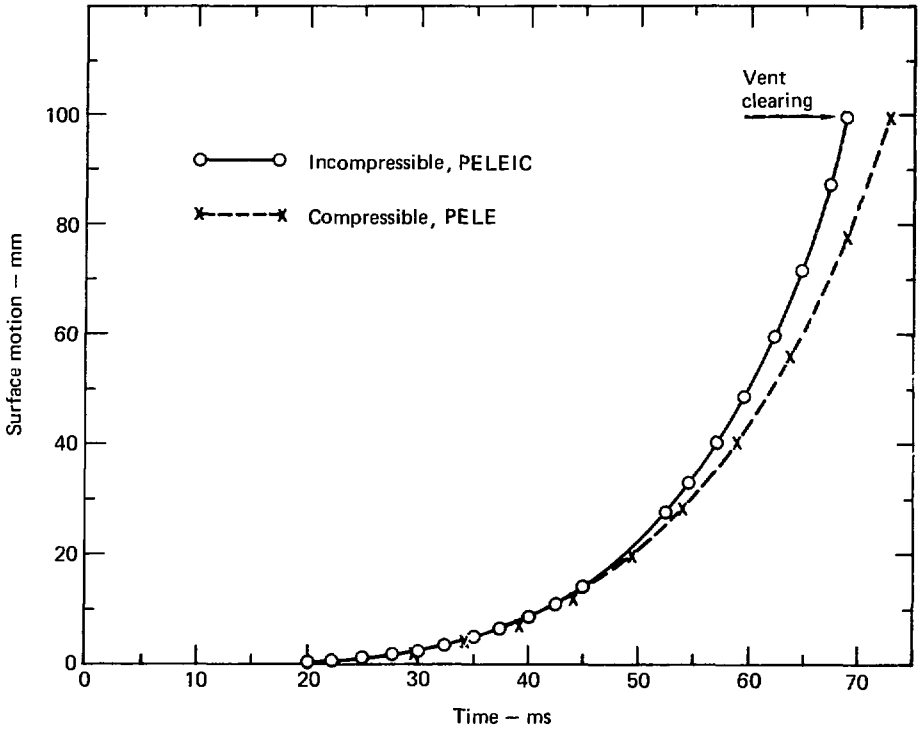

Fig. 15. Surface level in the downcomer UCLA experiment.

of the experimental determination. When we compare the initial download on the bottom of the flask, we find essentially no difference between the two calculations (Fig. 16). (The compressible result has been time shifted to match that of the incompressible calculation.) However, the computational time for the explicit approach becomes prohibitive (greater than 2 h), therefore the calculation was terminated. The incompressible calculation was carried out to about 120 ms using various time steps (δt) and convergence criteria (ϵ). These calculations typically required approximately 1 min of CDC-7600 time. Thus one sees that the incompressible approach gives the same answer and is capable of carrying the calculation to much later times in a more economical manner.

There are various methods that might be used to describe the bubble boundary: marker particles as used in the original MAC approach, polygonal boundaries as used in the highly versatile CHAMP code, or void fractions as used in either the SOLA-VOF or MAITAI codes. The approach used here was derived from my original efforts in the MAITAI code, and as modified for the two-phase PELE code. The resulting bubble description in the PELEIC code at 112 ms in the UCLA experiment is shown in Fig. 17. It is believed that the three methods should be approximately equivalent during the early stages of bubble growth. However, I believe that the void fraction approach will have less difficulty when the problem of bubble breakthrough of the surface is being modeled.

Further development of the PELEIC code is under way to extend its applicability to a wider range of problems and improve the basic assumptions used in the solution algorithms.

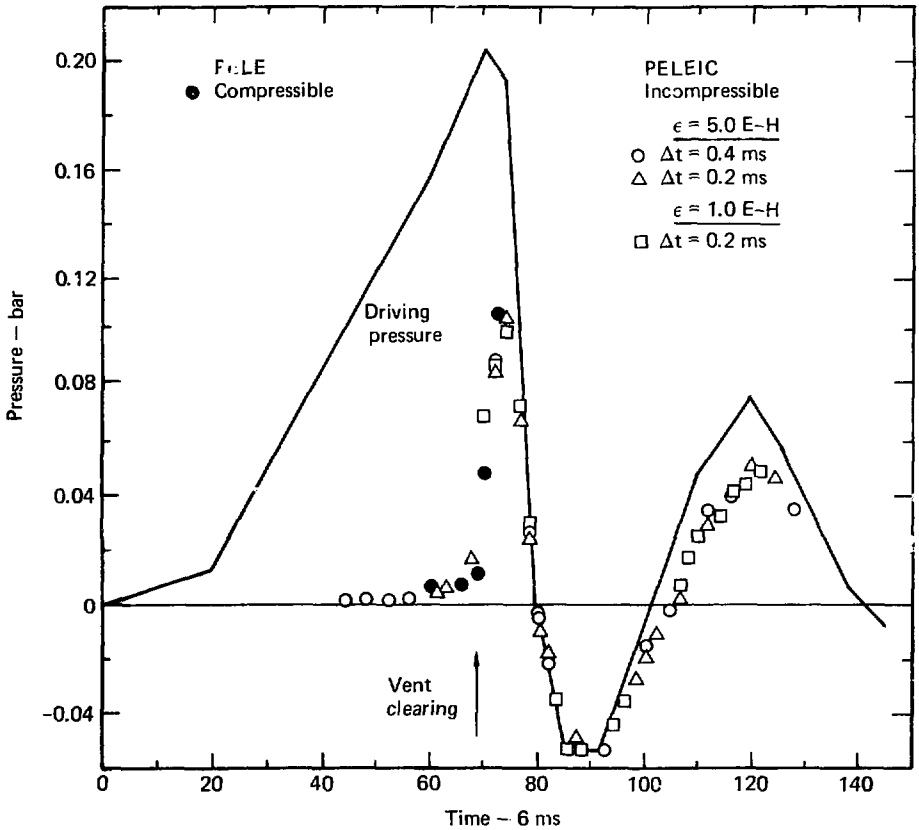

Fig. 16. Pressure time histories.

IV. FLUID DYNAMICS GROUP

(M. Ross, Group Leader)

The Fluid Dynamics Group is concerned with studying the detailed physics of fluids and the modeling of nonequilibrium rate-dependent constitutive properties such as turbulence, viscosity, electrical and thermal conductivity, and other transport properties that influence fluid flows. The group also carries out computer simulations of flows by using existing LLL codes, and developing new codes when necessitated by application.

The Model Potential Code

(M. Ross)

● **A new theoretical physics code has been developed to compute the equations-of-state and *transport properties of liquid metals and partially ionized dense plasmas.* This report summarizes an application of the code to lithium.**

Introduction

Over the past decade, pseudopotential theory has developed into a useful computational method

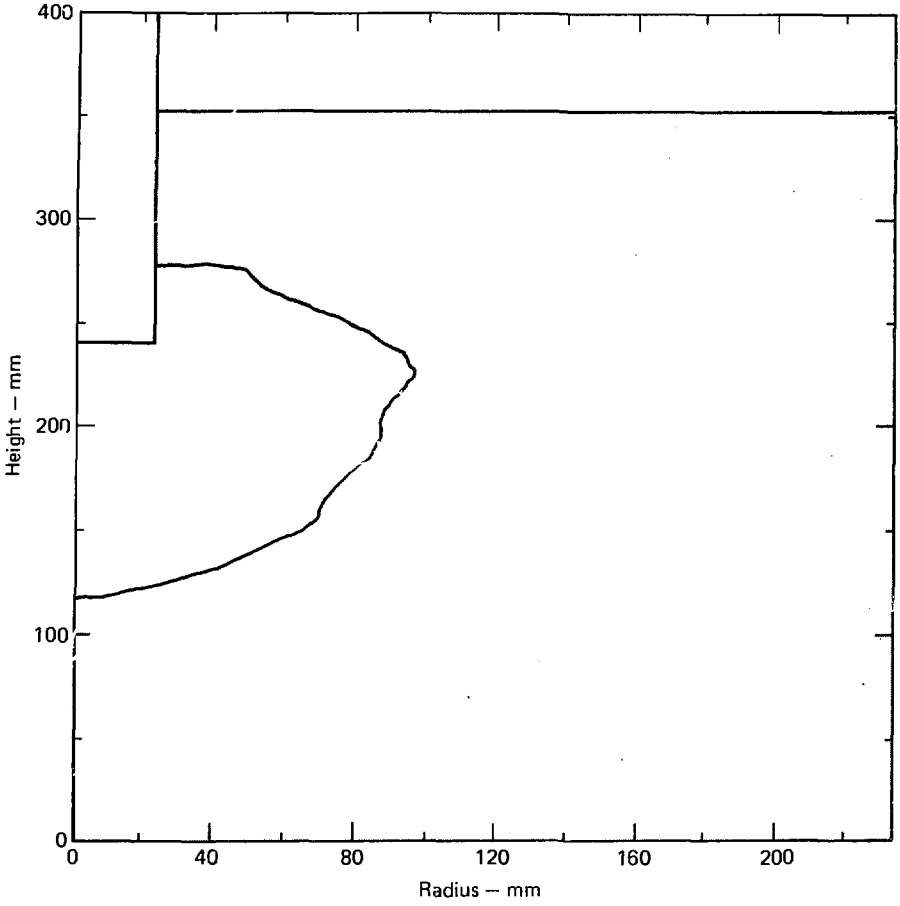

Fig. 17. Bubble profile at 112 ms in UCLA experiment.

leading to impressive progress in our understanding of material properties. Introduction of the pseudopotential method brought with it two important features. First, it allowed for a great simplification in the calculations of electronic properties of solids, permitting a minimal computational effort for accurate calculation of thermodynamic properties, electronic band structures and densities of states, and consequently optical, electrical, and magnetic properties. It also permitted the separation of electronic and ionic structural factors, thereby allowing the calculation of thermal properties of solids and liquids. The pseudopotential method has also found wide applicability in atomic and molecular physics, where it has been used to calculate electron energy levels, photon absorption or emission, electron scattering, and molecular properties.

In the most commonly applied form of the theory, which is the one used here, the physics of the

electron-ion attraction, electron-core repulsion, and the screening are modeled. Hence the name, Model Potential Code.

This report describes some of our work in applying the code to calculations of thermodynamic properties of liquid metals and partially ionized plasmas, with lithium as a specific illustration. The calculations were carried out to provide a complete equation-of-state data base for computer simulations of fusion reactor designs employing liquid lithium as a protective blanket and heat exchanger. A more complete summary of the lithium EOS is to be found in Sec. I in this report.

Summary of the Physics

Free energy. In this theory, the Helmholtz free energy can be written as

$$F = E_x + E_{corr} + E_x + E_{Coul}$$

$$+ \frac{2Z^2}{\pi} \int_0^\infty \frac{(V_\pi)^2}{(8\pi Z^2)^2} S(K)$$

$$\times \left(\frac{1}{\epsilon(K)}\right) - 1 \quad K^4 \, dK + F^0 + F_{EX} \, . \qquad (18)$$

The first three terms on the right side are the kinetic energy, correlation energy, and exchange energy of the free electron gas that is assumed to be in its ground state. These terms are independent of the ion positions. E_{Coul} is the Coulomb energy of the positive ions in the negative background and is given by

$$E_{Coul} = \frac{2Z^2}{\pi} \int_0^\infty [S(K) - 1] \, dK \, . \qquad (19)$$

S(K) is the liquid-structure factor. If we assume that the ions are arranged in the liquid as if they were hard spheres of diameter d, and that the structure factor can be approximated by using the Percus-Yevick theory, then E_{Coul} can be written analytically

$$E_{Coul} = - \frac{2Z^2}{\pi} \left(\frac{2\pi^2 d^2}{V} \frac{\frac{1}{2} - \frac{1}{10}\eta + \frac{1}{20}\eta^2}{1 + 2\eta} \right) , \qquad (20)$$

where $\eta = 1/6\pi d^3/V$. V is the atomic volume and energy is in rydbergs. The fifth term in Eq. (18) is the additional energy due to electron screening, and V_K is the model potential form factor to be discussed below. $F^\circ(d,V)$ is the free energy of the hard-sphere system of diameter d, and volume V and is

$$\frac{F^0}{NkT} = \frac{4\eta - 3\eta^2}{(1 - \eta)^2} \, . \qquad (21)$$

The thermodynamic properties are computed by finding the hard-sphere diameter that minimizes the free energy of Eq. (18), and then by evaluating the appropriate derivatives of the free energy to obtain the thermodynamic properties.

The last term, F_{ex} in Eq 18, represents the increase in the free energy due to electronic excitation of conduction and core electrons.

Model Potential. A commonly used functional form of V)K) is

$$V(K) = \left(- \frac{8\pi}{K^2} + \frac{\Omega}{\left(1 + K^2 r_c^2\right)^2} \right) , \qquad (22)$$

where Ω and r_c are adjustable parameters. $\epsilon(K)$ in Eq. (18) is the dielectric constant used in plasma physics. The dielectric constant here is similar to the Lindhard dielectric constant. However, it also includes corrections due to nonuniform electron gas exchange and correlation effects. The Ω and r_c used were obtained by fitting the theory to experimental values of the crystal binding energy, lattice spacing, and compressibility for body-centered cubic lithium at 100 K. Values of $\Omega = 23$ Ry au^3 and $r_c = 0.33$ au, were obtained and Z = 1. No attempt was made to optimize the potential parameters by fitting to the liquid data as well.

Results. Calculations of the properties of liquid lithium at low pressure near its melting point are in good agreement with experiment. In Fig. 18 we show the computed lithium Hugoniot along with experimental data. The calculations are in excellent agreement with the experimental work of Bakanova *et al.* [41] The origin of the discrepancy between the Soviet and Los Alamos Scientific Laboratory [42] work is unclear. Our calculations for sodium and aluminum (not shown) are in excellent agreement with experiments. Figure 19 compares the model potential predictions to those of the H-Division ACTEX code for the lithium isochore at V = 13.02 cm^3/mole, (the molar volume of the solid at room temperature) at temperatures from 0.1 to 30 eV.

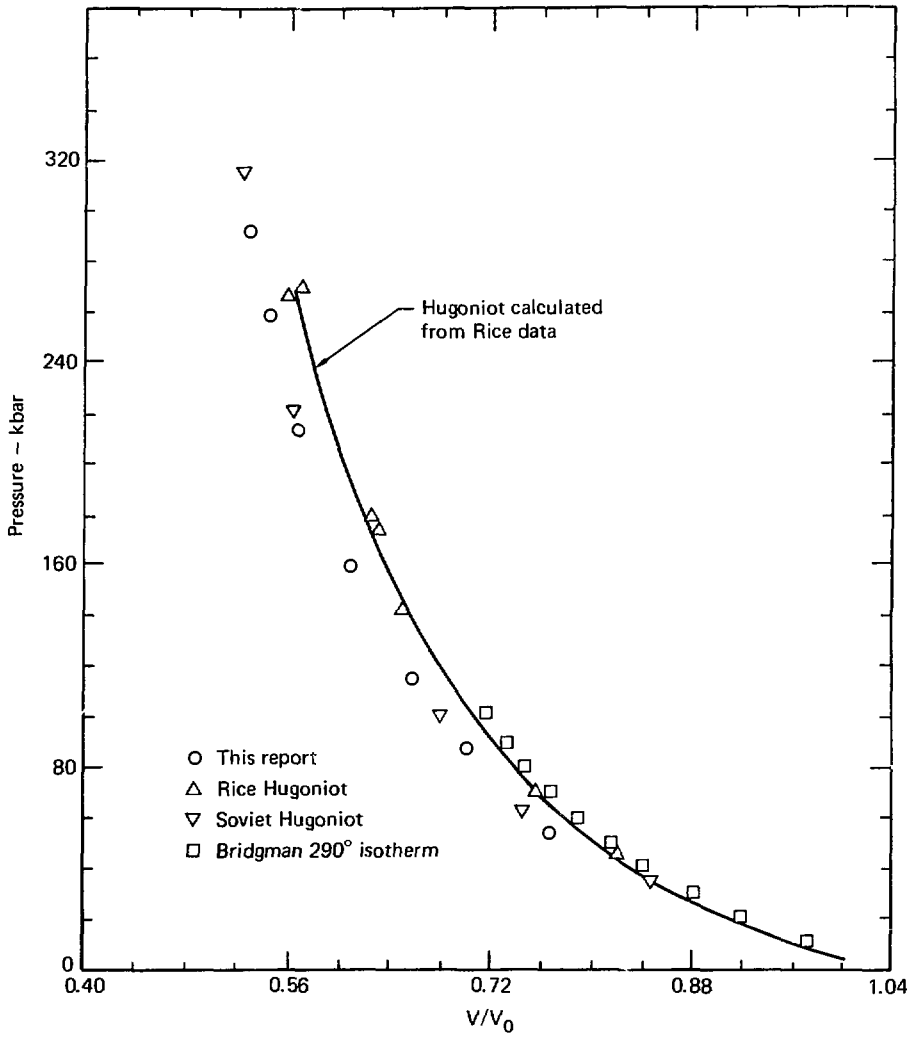

Fig. 18. Comparison of Bridgman isothermal compression data with shock data and calculated isotherms for lithium.

The ACTEX code is most valid at very high temperatures, or for fully ionized systems, and becomes of questionable applicability to lithium at temperature below 15 eV. The model potential calculations predict the correct low temperature experimental properties, and converge smoothly with ACTEX results in the temperature range over which ACTEX is valid. Above 30 eV, the disagreement between the two models never exceeds 10%.

Summary. The Model Potential Code is intended to correct a weakness in the H-Division EOS-code capability. At very high-temperatures the properties of plasmas can be adequately modeled by the ACTEX plasma code; at low temperature the

GRAY or soft-sphere molecular codes can be used to fit experimental data and provide reliable predictions. However, the large temperature range between the two, involving electronic excitation and partial ionization, is not being properly modeled; data have to be obtained here by extrapolating results of the two models and smoothing the fit over the intermediate temperature. The Model Potential Code, however, contains the appropriate physics to represent the liquid metal and partially ionized plasmas and, as illustrated in Figure 19, correctly predicts the limiting behaviors. Because it is essentially a metallic theory, the Model Potential Code is less adequate at densities below critical. However, at low densities, ACTEX and GRAY are quite adequate and have much less of a convergence problem. At very high densities, statistical models suffice.

Work underway on calculating the transport properties of lithium will be reported in a future quarterly.

Jet Stability in the Lithium Reactor System

(S. W. Kang)

● **In this section we analyze the fluid dynamic stability of the liquid-lithium waterfall blanket proposed for a laser fusion reactor design.**

A preliminary analysis is presented of the various hydrodynamic aspects involved in the stability of a liquid-lithium jet in a laser fusion reactor, which comprises a part of LLL's laser fusion power-generation concept.[43] Various physical factors that

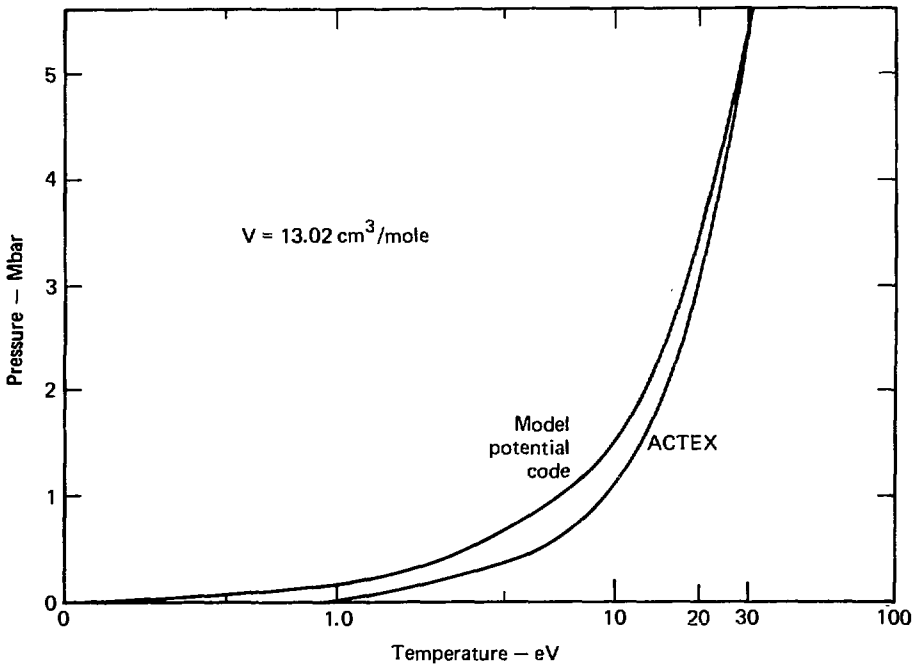

Fig. 19. Calculated lithium isochore at 13.02 cm^3/mole.

may affect the jet breakup are delineated, and some approximate analyses are performed to determine their relative influences. Areas of uncertainty are also pointed out, along with plans for experimental verification or further theoretical analysis.

The present reactor design calls for the chamber pressure to be 10^{-1} Torr, temperature 800 K, the chamber radius 5-m, the jet/sheet half-thickness 30 cm, and the exit jet velocity 10 m/s, yielding the Reynolds number $3(10^6)$ and the jet Weber number $4(10^4)$. The physical factors that may cause breakup of turbulent jets are the ambient conditions, the fluid properties, nozzle configurations, and possible vibrations of the reactor following pellet microexplosion.

Application of the criterion for the ambient effects [44] yields the result that the jet is insensitive to the present ambient conditions, i.e., the Weber number based on the chamber density is 10^{-3}, much lower than the critical value (5.3). However, it is not clear whether the presently designed low-density effects are negligible on the jet breakup behavior. Experiments are being conducted to reduce the degree of this uncertainty.

The fluid property effects on jet disintegration was considered in terms of the Ohnesorge number, which describes a measure of the relative importance of viscosity and surface tension in controlling stability. This number is $\sim 10^{-4}$, signifying dominant surface tension effect. It has been found [45,46] that surface tension tends to inhibit the growth of the irregular disturbances at the turbulent surface. However, recognizing the paucity of test data at very high Reynolds numbers, say 10^6, we plan to perform some experiments in this range.

With regard to the nozzle configuration effect on jet breakup, liquid sheets were observed to be more stable than circular jets from orifices of the same area. [47] In both situations there exist various profile patterns of the jet velocity, depending upon nozzle exit geometry. Moreover, the jet must undergo "relaxation" from a no-slip condition to a more uniform profile downstream. Additionally, the viscosity would affect this transitional behavior at the interface. An analysis is being conducted to determine the extent of its influence on the jet breakup behavior.

An estimate of the turbulent jet breakup length is based partly on empirical correlations, [48,49] which indicate a plateau value at high Reynolds numbers, a phenomenon similar to the laminar jet cases. Calculation yields the intact jet length well in excess of the presently designed 10 m, which appears to imply a stable turbulent jet flow for the laser fusion reactor. However, other physical factors may affect the jet breakup, as previously mentioned; therefore, this estimate should be considered preliminary, pending further investigation and experiments.

Turbulence Theory, Modeling, and Numerical Simulation

(A. C. Buckingham)

● The theme of the work discussed in this section is study and problem application of fluid dynamic turbulence theory. Three activities during the last quarter are part of this theme: (1) turbulence modeling and simulation in weapons design and effects analysis, (2) turbulence calculations and analysis for the rainout wind tunnel experiments, and (3) turbulence modeling and simulation in reactive (corrosive) and erosive flow environments. Each activity is identified with one or more LLL programs.

Turbulence Modeling and Simulation in Weapons Design and Effects Analysis

Four lectures were presented to nuclear weapons design and effects physicists in 1977 at LLL (October and November) and LASL (December). The purpose of these lectures was to introduce fundamental turbulence concepts in the framework of weapons physics applications.

An outgrowth of these lectures was organization of an LLL-LASL theoretical design team to examine turbulent mixing at an unstable material interface. Tentatively, we are examining extension of the Belen'kil-Frandkin [50,51] approach to include compressibility and a self-consistent description of turbulent entropy production at the interface. A Rayleigh-Taylor instability conceptually initiates the process at the interface, which is subjected to strong shock compression. We are seeking a numerical simulation of the developing Rayleigh-Taylor situation during shock propagation. We expect particular problem elements to include the equation of state of the mixing region, the thermodynamic description (including entropy production by turbulent mixing and heat transfer), and time-dependent definition of the interface. The governing mathematics will include Reynolds's equation, turbulence energy equation, and a modified equation of state for which we are currently considering use of the Onsager relations. Among the results we seek are a description of the time-dependent mixing zone, mass constituent mixing, temperature excursions, and altered growth rate of the mixing region. The new results should lead to experiments to test the theoretical description.

Turbulence Calculations and Analysis for the Rainout Wind Tunnel Experiments

The specific problem studied is that of droplet dispersion following flow-axis parallel injection in a prescribed (artificially generated) turbulent gas flow. We intend to measure the turbulence-enhanced attachment rate of aerosol debris particles to the injected droplets. Effects of the wind tunnel walls, droplet vaproization near heated walls, and spectrum energy characterization of the wind tunnel turbulence in comparison to the "natural" (unbounded atmospheric) situation must be modeled and theoretically "cancelled" from the experimental results. In this way the wind tunnel (artificial) aerodynamics can be quantitatively evaluated and removed from predictions about the Rainout attachment in the natural situation. This activity is supported by the D-Division Rainout program.

The numerical effort is split into three activities. First, spectral methods (the substitution of smooth Fourier functions for the random turbulent velocity spectrum distribution with wave length) are being developed to analyze hot-wire anemometry experiments, and to characterize the wind tunnel turbulence experiments. Second, the TEULER higher-order finite-difference solutions of the Navier-Stokes and turbulence closure model equations are being modified to explicitly simulate the wind tunnel jet-plate generated turbulence. Third, the kinetic BLIMP near-wall matrix code is undergoing modification to simulate the droplet-hot wall two-phase impingement and evaporation process. A paper is being prepared outlining these numerical methods for a multiphase flow workshop in February 1978. [52]

Turbulence Modeling and Simulation in Reactive (Corrosive) and Erosive Flow Environments

Revised formulation is underway for the BLIMP and TEULER codes, a composite implicit-explicit integral finite-difference method, and the NEST nonequilibrium chemical kinetics flow code for study of gun barrel erosion. This work is being supported by LLL's nonnuclear ordinance program. A new, comprehensive study of the fundamental mechanisms responsible for erosion/corrosion of gun barrel liner materials was the subject of an interdisciplinary laboratory proposal for which we are initiating this numerical method development. [53] In advance of the proposal award, the plan is to model and analyze approximately 15 months of accumulated experimental results from the LLL Chemical and Material Sciences Division's hot gas erosion program.

REFERENCES

1. D. A. Young, Lawrence Livermore Laboratory, report in preparation.
2. M. Ross, Lawrence Livermore Laboratory, report in preparation.
3. F. J. Rogers, *Phys. Rev.* **A9**, 2441 (1974).
4. F. J. Rogers, *Phys. Lett.* **61A**, 358 (1977).
5. H. E. DeWitt, *J. Math. Phys.* **3**, 1216 (1962).
6. C. Deutsch and M. M. Gombert, *J. Math. Phys.* **17**, 1077 (1976).
7. S. L. McCarthy, *The Kirzhnitz Corrections to the Thomas-Fermi Equation-of-State*, Lawrence Livermore Laboratory, Rept. UCRL-14363 (1965); K. Johnson, Lawrence Livermore Laboratory, Internal Document, HTN-252 (1976). Readers outside the Laboratory who desire further information on LLL internal documents should address their inquiries to the Technical Information Department, Lawrence Livermore Laboratory, Livermore, California 94550.
8. D. T. Warren, *Nuclear Corrections for Genesis*, Lawrence Livermore Laboratory Rept. UCID-15316 (1968).
9. R. Grover, Lawrence Livermore Laboratory, Internal Document HTN-259 (1976).
10. R. Grover, *High Temperature Equation of State for Simple Metals*, Lawrence Livermore Laboratory, Rept. UCRL-79505 (1977).
11. V. P. Kopyshev, *Sov. Phys.-Doklady* **10**, 338 (1965).
12. R. Grover, Lawrence Livermore Laboratory, unpublished work.
13. E. L. Pollock and J. P. Hansen, *Phys. Rev.* **A8**, 3110 (1973).
14. E. Royce, *GRAY, A Three-Phase Equation of State for Metals*, Lawrence Livermore Laboratory, Rept. UCRL-51121 (1971).
15. R. Grover, "High-Temperature Equation of State for Simple Metals," in *Proc. of Seventh Symp. on Thermophysical Properties*, Gaithersburg, MD. (1977), to be published.
16. D. A. Young and B. J. Alder, "Critical Point of Metals from the Van der Waals Model," in *Phys. Rev.* **A3**, 364-371 (1971).
17. D. J. Steinberg, "A Simple Relationship between the Temperature Dependence of the Density of Liquid Metals and their Boiling Temperatures," in *Metall. Trans.* **5**, 1341-1343 (1974).
18. L. B. Evans, B. L. Hord, A. C. Mitchell, and M. Van Thiel, *A New Die-Cast Projectile Design for Two-Stage Light-Gas Guns*, Lawrence Livermore Laboratory, Rept. UCRL-51664 (1974).
19. G. R. Gathers, J. W. Shaner, C. A. Calder, and W. W. Wilcox, *Determination of Sound Velocity in Liquid Metals at Temperatures Above 4000 K*, Lawrence Livermore Laboratory, Rept. UCRL-79322 (1977).
20. R. Grover, *J. Chem. Phys.* **55**, 3435 (1971).
21. W. G. Hoover, S. G. Gray, and K. Johnson, *J. Chem. Phys.* **55**, 1128 (1971).
22. G. Grimwall, *Phys. Script* **14**, 63 (1976).
23. K. Gschneidner "Physical Properties and Interrelationships of Metallic and Semimetallic Elements," in *Solid State Physics*, Seitz and Turnbull, Eds. (Academic Press, New York, 1964) Vol. 16.
24. W. McMillan, *Phys. Rev.* **167**, 331 (1968).
25. B. Bosacchi and P. Franzosi, *Phys. Stat Sol* **b77**, 457 (1976).
26. S. D. Bader and G. S. Knapp, *Phys. Rev.* **B11**, 3348 (1975).
27. L. F. Mattheiss, *Phys. Rev.* **B1**, 373 (1970).
28. W. H. Butler, *Phys. Rev.* **B15**, 5267 (1977).
29. L. F. Mattheiss, *Phys. Rev.* **139**, A1893 (1965).
30. C. M. B. Webber and R. W. B. Stephens, "Transmission of Sound in Molten Metals," in *Physical Acoustics*, W. P. Masin, Ed. (1968), Vol. IV *B* p. 53.
31. A. F. Crawley, *Int. Met. Revs.* **19**, 32 (1974).
32. R. Hultgren, P. D. Resai, D. T. Hawkins, M. Gleiser, K. K. Kelley, and D. D. Wagman, "Selected Values of Thermodynamic Properties of the Elements," *Am. Soc. Met.*, (1973).
33. J. W. Shaner, G. R. Gathers, and W. M. Hodgson, *Thermophysical Measurements on Liquid Metals above 4000 K*, Lawrence Livermore Laboratory, Rept. UCRL-78782 (1977).
34. R. Grover, *High Temperature Equation of State for Simple Metals*, Lawrence Livermore Laboratory, Rept. UCRL-79505 (1977).
35. G. R. Gathers, J. W. Shaner, R. L. Brier, *Rev. Sci. Instr.* **47**, 471-479 (1976).

36. Y. Waseda, K. Hirata, M. Ohtani, *High Temperatures-High Pressures* **4**, 221-226 (1975).
37. A. V. Vertogradskii, *High Temp.* **15**, No. 1, pp. 178-180, Jan.-Feb. 1977.
38. G. Birkhoff *et al.* "Explosives with Lined Cavities," in *J. App. Phys.* **19**, 563 (1948).
39. C. W. Hirt, B. D. Nichols, and N. C. Romero, *SOLA — A Numerical Solution Algorithm for Transient Fluid Flows*, Los Alamos Scientific Laboratories, Los Alamos, N.M. Rept. LA-5852 (1975).
40. I. Catton, C K. Chan, K. Dhir, H. H. Chiou, and C. K. B. Lee, *Suppression Pool Dynamics*, University of California at Los Angeles (1977).
41. A. A. Bakanova, I. P. Dudoladov, and R. F. Trunin, *Sov. Phys. Solid St.* **7**, 1407 (1965).
42. M. H. Rice, *J. Phys. Chem. Solids* **26**, 483 (1965).
43. J. A. Maniscalco and W. R. Meier, *Conceptual Design of a Laser Fusion Power Plant*, Lawrence Livermore Laboratory, Rept. UCRL-79652 (1977).
44. R. W. Fenn and S. Middleman, "Newtonian Jet Stability: the Role of Air Resistance," *in Am. Inst. Chem. Eng.* **15**, No. 3, 379-383 (1969).
45. J. T. Davies, *Turbulence Phenomena* (Academic Press, New York, 1972).
46. A. A. Townsend, "The Mechanism of Entrainment in Free Turbulent Flows," in *J. Fl. Mech.* **26**, Pt. 4, 689-715 (1966).
47. R. P. Fraser, P. Eisenklam, and N. Dombrowski, "Drop Formation from Rapidly Moving Liquid Sheets," *in Am Inst. Chem. Eng.* **8**, No. 5, 672-680 (1962).
48. R. E. Phinney, "The Breakup of a Turbulent Liquid Jet in a Gaseous Atmosphere", in *J. Fl. Mech.* **60**, Pt. 4, 689-701 (1973).
49. T. Kusui, "Liquid Jet Flow into Still Gas," in *Bull. JSME*, **11**, No. 48, 1084-1090 (1968).
50. S. Z. Belen'kii, and E. S. Fradkin, "Theory of Turbulent Intermixing," in *Quantum Field Theory and Hydrodynamics, Proc. of P.N. Lebedev Physics Inst.* (**29**) Ed. D. V. Skobel'tsyn (1967), pp. 197-229.
51. E. S. Fradkin, "Investigation of the Stability of Arbitrary One-Dimensional Hydrodynamical Flow", in *Quantum Field Theory and Hydrodynamics, Proc. of P.N. Lebedev Physics Inst.* (**29**) Ed. D. V. Skobel'tsyn (1967), pp. 243-249.
52. A. C. Buckingham, "Wind Tunnel Wall Coating by Liquid Droplets Injected in High Speed Turbulent Gas Flow," Invited paper to be given at *ARO Workshop on Multi-Phase Flows*, Ballistic Research Lab. (Aberdeen Proving Ground, Md. (1978).
53. A. C. Buckingham, F. P. Milanovich, D. W. Short, and W. J. Siekhaus, *An Investigation of the Mechanics of Hot, Multi-Phase Erosion/Corrosion Phenomena*, Lawrence Livermore Laboratory, Rept. LLL-Prop-150 (1977).

RMD